Volume 1 | Number 1 | Jan 2013 | Pages 1–100

Journal of
Materials Chemistry A

Materials for energy and sustainability
www.rsc.org/materialsA

Li⁺

ROYAL SOCIETY
OF CHEMISTRY

ROYAL SOCIETY
OF CHEMISTRY

www.rsc.org/materialsA

In-Situ High-Energy Synchrotron X-ray Diffraction Studies and First Principles

Modeling of α-MnO$_2$ Electrodes in Li-O$_2$ and Li-ion Coin Cells

Zhenzhen Yang,[a,] Lynn Trahey,[a] Yang Ren,[b] Maria K. Y. Chan,*[c] Chikai Lin,[a]

John Okasinski,[b] and Michael M. Thackeray[a]

[a]*Chemical Sciences and Engineering Division*
[b]*X-ray Science Division, Advanced Photon Source*
[c]*Center for Nanoscale Materials*
Argonne National Laboratory, 9700 South Cass Avenue, Argonne, IL 60439, USA

*Corresponding author: **Maria Chan (mchan@anl.gov)**

Abstract

Despite their technological challenges, non-aqueous rechargeable lithium-oxygen cells offer extremely high theoretical energy densities and are therefore attracting much attention in a rapidly emerging area of electrochemical research. Early results have suggested that, among the transition metal oxides, alpha manganese dioxide (α–MnO$_2$) appears to offer electrocatalytic properties that can enhance the electrochemical properties of Li-O$_2$ cells, particularly during the early cycles. In this study, we have investigated the hybrid Li-ion/Li-O$_2$ character of α–MnO$_2$ electrodes in Li-O$_2$ coin cells by in-situ high-energy synchrotron X-ray diffraction, and compared the results with conventional Li/α–MnO$_2$ coin cells assembled under argon. Complementary first principles density functional theory calculations have been used to shed light on competing lithium insertion and lithium and oxygen insertion reactions within the α–MnO$_2$ tunnel structure during discharge, relative to lithium peroxide or lithium oxide formation.

1

1. Introduction

Electrochemical Li-O$_2$ cells have attracted substantial attention in recent years because their high intrinsic energy density (about 3600 and 5200 Wh/kg for Li/Li$_2$O$_2$ and Li/Li$_2$O cells, respectively, based on the mass of the active electrode materials only) can potentially meet the requirement for electric vehicle applications.[1-3] A key component of the cell is the porous oxygen electrode (the cathode). Because the oxygen-oxygen bond is not completely severed during the electrochemical formation of lithium peroxide, Li$_2$O$_2$, this partial discharge reaction is, in principle, reversible;[2, 3] this reaction is therefore preferred to the full discharge reaction that generates the Li$_2$O structure in which the oxygen ions form a cubic-close-packed array.[4] In practice, the O$_2$ electrode is limited by 1) sluggish kinetics of the oxygen reduction/oxidation reactions, 2) undesired side reactions, e.g., with electrolyte solvents, and 3) inefficient design,[5-7] all of which influence the power and energy output, as well as the energy efficiency of the cell. For example, current Li-O$_2$ cells are typically charged at 0.1-0.5 mA/cm^2, whereas Li-ion batteries can be typically charged at >10 mA/cm^2.[7, 8] Furthermore, the potential difference between charge and discharge reactions in Li-O$_2$ cells is often greater than 1.0 V, which results in a low energy efficiency (typically <60%) relative to Li-ion cells (>90%).[7] Thus, there is a pressing need for efficient and effective electrocatalysts to improve the rate of O$_2$ reduction and oxidation reactions, thereby reducing high overpotentials, particularly during charge.

Prior research has suggested that transition metal oxides, particularly manganese oxides and iron oxides, are promising candidates as electrodes/electrocatalysts for Li-O$_2$ cells, and that MnO$_2$, in particular, improves the reversibility and lowers the overpotential during charge and discharge.[9-12] In fact, MnO$_2$ is not new to the lithium battery community; it has served as an insertion electrode in primary and rechargeable lithium batteries for many years.[13-19] Nonetheless, its function in Li-O$_2$ cells has still to be explored in detail.

Research of various manganese oxides by Bruce and others[10, 20, 21, 22] has demonstrated that, when used in $Li-O_2$ cells, the crystal structure and morphology of the MnO_2 electrode/electrocatalyst have a significant effect on the electrochemical behavior of the cells. One polymorph in particular, $\alpha-MnO_2$, which has a hollandite-type structure with relatively large, one-dimensional '2×2' tunnels formed by the connection of octahedral $[MnO_6]$ units, operates as a superior catalyst in $Li-O_2$ cells relative to other MnO_2 polymorphs, such as $\beta-MnO_2$ nanowires with narrow 1-D '1×1' tunnels (rutile-type structure) and $\delta-MnO_2$ nanosheets with a two-dimensional, layered-type structure.[10, 20, 17, 21] These authors have proposed that the open framework of the $\alpha-MnO_2$ structure plays a key role in the electrochemical reaction, because both intercalated lithium ions and lithium-oxide discharge products can be incorporated in, and removed from, the interstitial space of the $\alpha-MnO_2$ framework during discharge and charge, respectively.[8,10,13] Note that the lithium-ion reactions would be accompanied by partial redox of the manganese ions, thereby giving the $\alpha-MnO_2$ hybrid electrode/electrocatalyst (or Li-ion/$Li-O_2$ character). However, it is not yet clear how the structural changes in $\alpha-MnO_2$ electrodes/electrocatalysts relate to reversible Li^+-ion insertion and extraction reactions and/or to O_2 reduction and oxidation (evolution) reactions, respectively.

The development of *in situ* powder X-ray diffraction techniques, particularly with synchrotron radiation sources, has significantly advanced our understanding of the structural evolution of electrodes during electrochemical cell cycling.[23-25] The availability of high flux, high energy synchrotron X-rays allows structural changes of electrochemically active materials in complex environments to be probed quickly and in great detail. The ability to obtain both structural and electrochemical information in real time and in a synchronized manner, and the advantage of comparing multiple measurements from the same sample, has provided a clearer picture about the mechanisms which govern the electrochemical processes that take place in

electrode materials. In this study, *in situ* X-ray diffraction (XRD) measurements were obtained

on α-MnO$_2$ electrodes when operated under argon in standard lithium cells, and under oxygen in

Li-O$_2$ cells. In both types of cells, the XRD data provides evidence of systematic changes to the

α-MnO$_2$ structure on cycling that correspond to lithium/lithium oxide insertion/extraction,

whereas the electrochemical profiles of the Li-O$_2$ cells suggest that oxygen reduction/oxidation

also occurs, which includes Li$_2$O$_2$ (or Li$_2$O) formation during discharge, consistent with the

concept of a hybrid electrode system.

2. Experimental and Computational Methods

2.1 MnO$_2$ synthesis

α-MnO$_2$ was synthesized from a Mn$_2$O$_3$ precursor that was prepared by heating

electrolytic manganese dioxide (Energizer) in air at 700 °C for 24h. Refluxing the Mn$_2$O$_3$

precursor in 4.5M H$_2$SO$_4$ for 16 h at 60 °C yielded a dark brown product which was then filtered

and rinsed with deionized H$_2$O. The product was dried in an oven at 275 °C for 16h before being

used as the cathode in lithium coin cells. A thermogravimetric analysis (TGA) was obtained for a

partially hydrated sample heated at 275 °C and stored in a desiccator for several months, and a

freshly heated sample at 275 °C. The samples were heated from room temperature to 700 °C at a

rate of 5 °C/min using a NETZSCH instrument (mode: TG 449 F3 Jupiter). The experiment took

place in compressed air gas with flow rate of 60ml/min.

2.2 Cell design

Li-O$_2$ coin cells (size 2032) with X-ray transparent windows were specifically designed

and constructed to study real-time electrochemical processes at Argonne's Advanced Photon

Source and to monitor, *in situ*, phase changes at the oxygen electrode during electrochemical

cycling. A schematic representation of the cell is shown in Figure 1a. Porous cathodes consisted

of 32% α-MnO$_2$, 41% PVdF binder, and 27% conductive carbon. The cathode laminates were made by mixing a slurry of the solid components in a 4:1 ratio of dry acetone and propylene carbonate, respectively, casting the slurry onto glass and, thereafter, drying and cutting the thin film into a disc electrode, ½" in diameter. A lithium foil disc was used as the counter electrode and separated from the MnO$_2$-carbon disc by two layers of quartz fiber (Whatman QMA) to prevent internal shorting. The electrolyte was a 1M solution of LiTFSi in tetraethylene glycol dimethyl ether, CH$_3$O-(CH$_2$CH$_2$O)$_4$-CH$_3$ (TEGDME) purified through standard measures to minimize water.
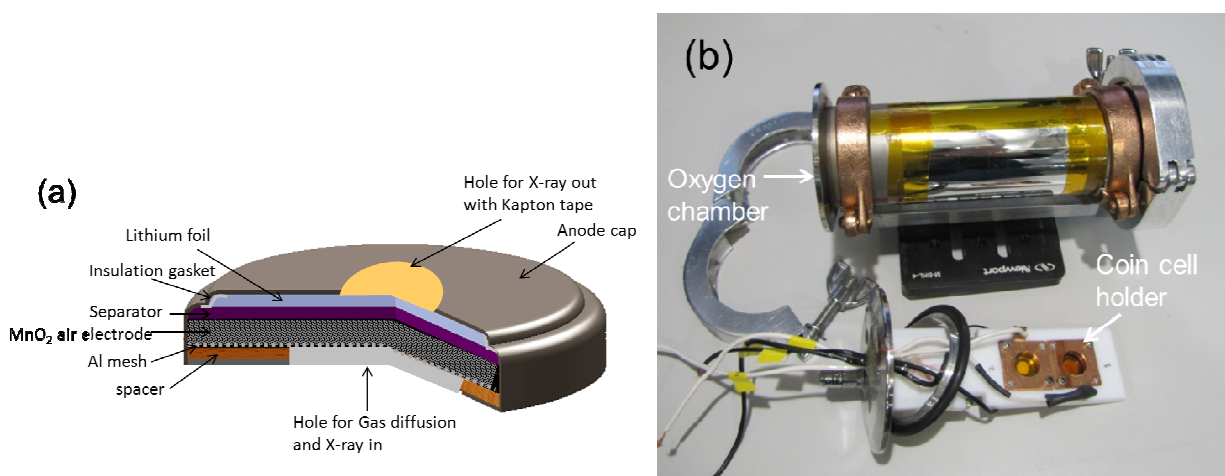
Figure 1. Schematic view of (a) a coin cell and (b) the oxygen chamber used for the *in situ* X-ray experiments. A copper holder was used to house the coin cell within the chamber that had airtight aluminized mylar windows through which the X-rays passed during the experiments.

A glass chamber (Figure 1b) to house the Li-O$_2$ cell was designed and manufactured as follows: A stainless steel cylinder, 5 cm in diameter, was sealed on both ends by O-rings and stainless steel clamps. Gas inlets and outlets and electrical circuits were accommodated in the plates. Circular holes, approximately 7 mm in diameter in the cathode can and 3 mm in diameter in the anode lid of the coin cell, permitted transmission of the X-rays through the entire cell; the lid was covered by a thin Kaplon tape, whereas the base of the can remained open, the electrolyte being contained within the cell by wicking to separator fibers, the MnO$_2$-carbon electrode and a

porous Al mesh at the base of the cell (Figure 1a). The coin cell was contained in a copper holder

which, in turn, was embedded in a Teflon plate to prevent the possibility of short circuiting. Two

aluminized mylar foil windows in the chamber were aligned in the direction of the X-ray beam

and detector. A more detailed description of the cell design and chamber is provided in a recent

paper by Ryan et al.[26] Coin cells were assembled and sealed in the chamber in an Ar-filled glove

box. After removal from the glove box, the chamber was purged with O_2 for 40 min through the

inlet and outlet ports, and allowed to soak for 2 hrs.

Standard Li/α-MnO$_2$ coin cells (also size 2032) were assembled, using the same

TEGDME electrolyte and sealed under argon for comparative electrochemical evaluation.

2.3 Electrochemical Cycling

Both Li/α-MnO$_2$–O$_2$ and standard Li/α-MnO$_2$ (Ar) coin cells were charged and

discharged at 0.05 mA at room temperature and electrochemically controlled by a MACCOR

battery cycler. For the first two cycles, the Li/α-MnO$_2$–O$_2$ cell was first discharged for 10 h and

then charged for 10 h before being discharged to 2.0 V without a time limitation, and finally

charged for 7h before termination of the *in situ* experiment. The Li/α-MnO$_2$ (Ar) coin cell was

subjected to only one discharge to 2.2 V and a single charge to 4.4 V to monitor differences in

the voltage profiles of the two types of cell, for comparison.

2.4 In situ X-ray measurements

XRD patterns were collected continuously using a high-energy synchrotron X-ray beam

(20.49 keV, wavelength 0.60505Å) at Sector 1-BM-B of the Advanced Photon Source at

Argonne National Laboratory. The diffraction scans were typically 5 min in duration with a

relatively long 30 min intermission between scans to reduce X-ray damage to the samples. A

Perkin-Elmer large area detector covered the 0-40° 2θ range of the complete scan. For most

figures, the two-dimensional diffraction patterns were calibrated and converted to a conventional

intensity vs. 2θ format using the program Fit2D.[27] XRD patterns of the α-MnO$_2$ electrode powders were collected to determine and confirm the purity of the materials. The software package GSAS with the EXPGUI interface was used for Rietveld refinements of unit cell and other structural parameters.[28, 29]

2.5 First principles density functional theory calculations

Density functional theory (DFT) calculations of the parent and various lithiated and Li$_2$O-containing α-MnO$_2$ structures were performed using the plane wave code VASP,[30] with supplied projector augmented wave (PAW) potentials.[31] The soft version of the PAW potential for oxygen was used. To treat the exchange-correlation, the generalized gradient approximation (GGA) of Perdew-Becke-Ernzerhof[32] (PBE) with the Hubbard-U correction in the implementation of Dudarev et al.[33] was employed. The value of U was chosen to be 3.5 eV in order to reproduce experimental formation enthalpies of 5 compounds in the Li-Mn-O system.[34] Kinetic energy cutoffs of 350 eV for the plane wave basis set, and Γ-centered grids of 8000 Å^3/V k-points, where V is the volume of the computational cell, were used. The cell parameters and the internal coordinates of the atoms were relaxed until the total energy converged to 0.1 meV/cell, and then re-relaxed to ensure the consistency of plane wave basis set.

3. Results and Discussion

3.1 The α-MnO$_2$ Structure

α-MnO$_2$ exists in nature in several mineral forms;[35] it has a 2×2 tunnel structure which is typically stabilized by cations at the center of the tunnels such as Ba^{2+} (hollandite) and K$^+$ (cryptomelane), as shown schematically in Figure 2a. The presence of these cations results in a slight reduction of the manganese ions for charge balance. It has also been demonstrated that the tunnel can be occupied by NH$_4^+$ [36] or H$_3$O$^+$ (or H$_2$O),[15] in which case the center of the tunnel is

occupied by a negatively charged N^{3-} or O^{2-} anion, respectively. The water in the tunnel can be replaced through an ion-exchange process to produce a Li_2O-stabilized product (Figure 2b).[13, 37]

(a)   (b)
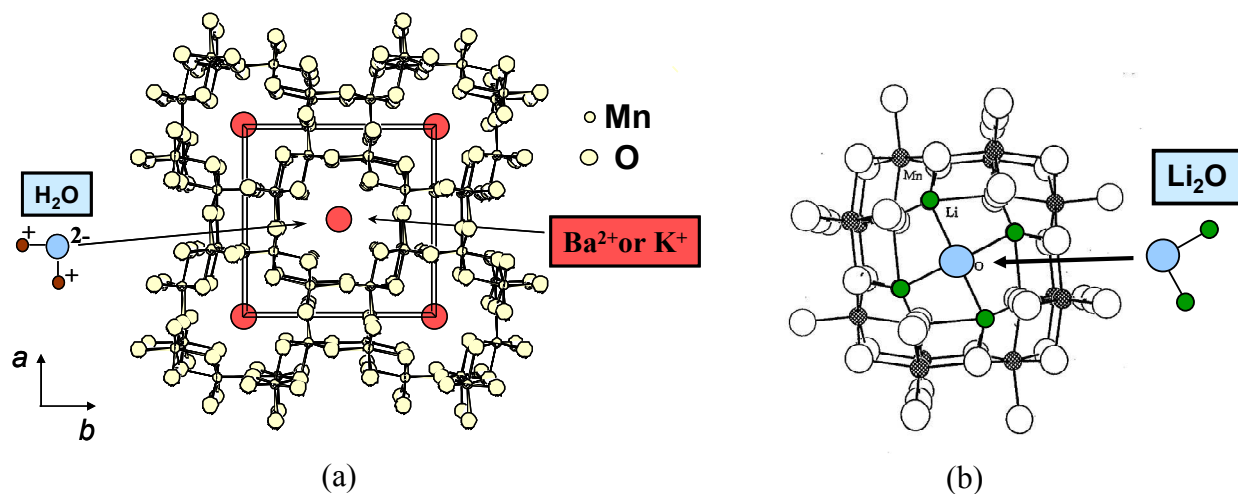
Figure 2. The structures of α-MnO₂ as represented by the minerals (a) hollandite (Ba-stabilized) and cryptomelane (K-stabilized)[38] and (b) lithia-stabilized α-MnO₂ [13].

The amount of stabilizing cationic or anionic species appears to be essentially constant throughout the series of α-MnO₂ (Mn_8O_{16}) compounds, i.e., between 1.2 and 1.6 per Mn_8O_{16} units for $Ba_{1.2}Mn_8O_{16}$,[39] $K_{1.3}Mn_8O_{16}$,[36] $Rb_{1.3}Mn_8O_{16}$,[36] $(NH_4)_{1.4}Mn_8O_{16}$,[36] and $(H_2O)_{1.6}Mn_8O_{16}$.[15] When hydrated α-MnO₂ is ion-exchanged with lithium, an X-ray refinement of the structure has yielded the composition $0.15Li_2O{\bullet}MnO_2$,[13] or $(Li_2O)_{1.2}Mn_8O_{16}$, in general agreement with the composition of related compounds structures, indicating that α-MnO₂ tunnel structures are stabilized, in general, by approximately 0.15 to 0.20 cations or anions, located at the tunnel center, per formula unit.

3.2 Structural Characterization of Hydrated and Dehydrated α-MnO₂

The powder XRD patterns of two partially hydrated (275°C) samples and one dehydrated (400 °C) α-MnO₂ sample are shown in Figure 3. The patterns are remarkably similar, suggesting that the size of the 2×2 cavity is largely unaffected by the dehydration process. The refined

lattice parameters, together with the water content of the samples, as determined from the TGA

plots in Figures 4a and b, are listed and compared with data from earlier work in Table 1.
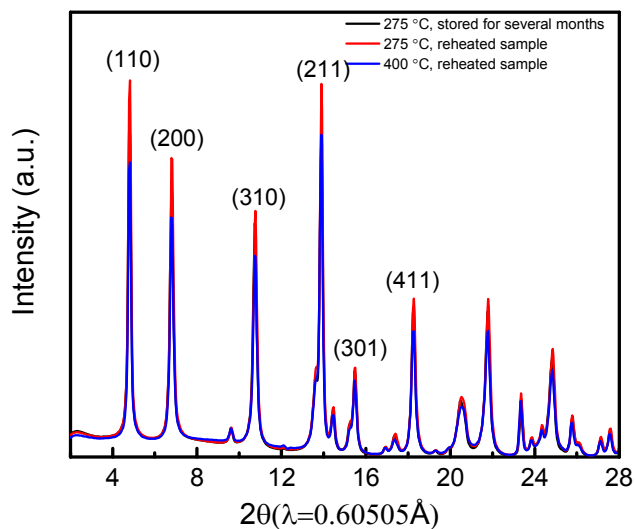
Figure 3. Synchrotron XRD patterns (λ=0.60505Å) of partially dehydrated and fully dehydrated α-MnO$_2$.
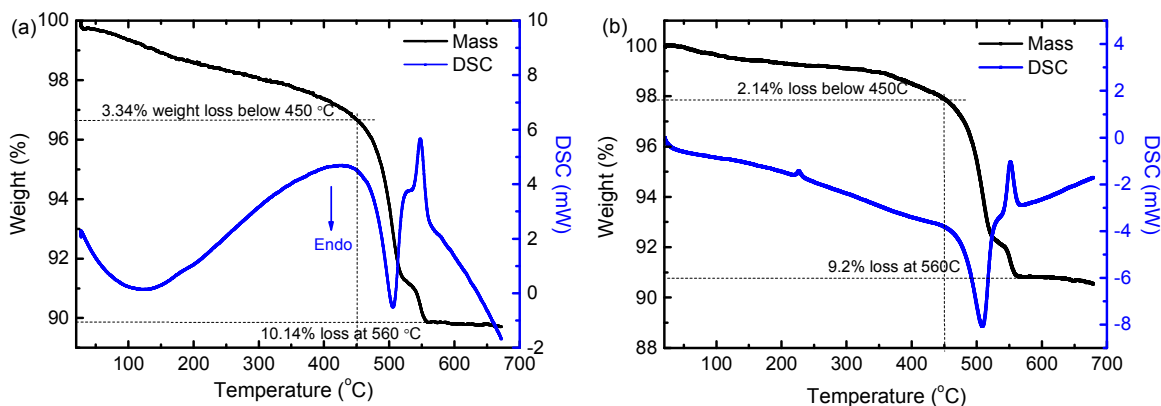
Figure 4. TGA data of two partially dehydrated α-MnO$_2$ samples: (a) after heating at 275 °C and stored in a desiccator for several months, and (b) a freshly heated sample at 275 °C.

Previously reported data have shown that hydrated α-MnO$_2$ samples, after drying at 100

°C, typically contain about 0.3H$_2$O per MnO$_2$ unit,[15] which is associated with both surface- and

lattice water (Table 1). The TGA data of the sample that had been initially dried at 275 °C and

stored in a desiccator for several months (Figure 4a) showed a weight loss of about 0.83 wt%

below 120 °C, corresponding to $0.04H_2O \bullet MnO_2$, which was attributed to the desorption of weakly adsorbed surface water; the lattice water released between 120 and 450 °C was 2.51 wt %, corresponding to $0.13H_2O \bullet MnO_2$, thus yielding a total water content of the parent sample of $0.17H_2O \bullet MnO_2$. The TGA data of the freshly heated sample showed that the H_2O content was $0.11H_2O$ (Figure 4b), i.e., lower than that of the stored sample, indicative of the tendency for dehydrated samples to re-absorb the lost water. Above 450 °C, the samples lose oxygen and transform to Mn_2O_3, as already described by others.[13, 15]

Table 1. Variation in the unit cell parameters of tetragonal α-MnO_2-based materials

Reference/ Composition	Description	a (Å)	c (Å)	Vol. (Å^3)
Rossouw et al.[15]				
$0.3H_2O \bullet MnO_2$ (lattice and surface H_2O)	hydrated, as prepared, TGA analysis (H_2O), XRD	9.7799	2.8534	272.92
$0.2H_2O \bullet MnO_2$ (lattice water only)	hydrated, as prepared, neutron refinement (O)	9.7826	2.8573	273.44
α-MnO_2	dehydrated at 300 °C, XRD neutron refinement (O)*	9.7851 9.7876	2.8627 2.8650	274.10 274.45
Li_xMnO_2	discharged electrode, XRD	10.039	2.8539	287.62
Rossouw et al.[37]				
'$0.12Li_2O \bullet MnO_2$'	Li ion-exchanged, XRD	9.844	2.85	276.18
Johnson et al[13]				
$0.33H_2O \bullet MnO_2$	hydrated, as prepared, TGA, H-analysis, XRD	9.8107	2.8502	274.33
α-MnO_2	dehydrated at 275 °C, XRD	9.7502	2.8607	271.96
$0.05Li_2O \bullet MnO_2$	Li ion-exchanged, XRD	9.8180	2.8595	275.64
$0.10Li_2O \bullet MnO_2$	Li ion-exchanged, XRD	9.9035	2.8531	279.83
$0.15Li_2O \bullet MnO_2$	Li ion-exchanged, XRD	9.9646	2.8499	282.98
$Li_{0.26}(0.15Li_2O \bullet MnO_2)$	chemically-lithiated product (LiI, 25 °C), XRD	10.169	2.846	294.30
$Li_{0.42}MnO_2$	chemically-lithiated product (LiI, 25 °C), XRD	10.039	2.852	287.43
This work				
$0.17H_2O \bullet MnO_2$	dehydrated at 275 °C stored in dessicator (mths) 1st TGA analysis (H_2O), synchrotron XRD	9.7914	2.8633	274.51
$0.11H_2O \bullet MnO_2$	dehydrated at 275 °C 2nd TGA analysis (H_2O), synchrotron XRD	9.7732	2.8639	273.55
α-MnO_2	dehydrated at 400 °C, *in situ* synchrotron XRD	9.8138 9.79*	2.8754 2.87*	276.93 275*

*Values estimated for 25 °C from the 400 °C *in situ* measurements and the thermal expansion coefficients of β-MnO_2.[40]

The *a* and *c* lattice parameters of the partially hydrated and dehydrated α-MnO$_2$ tetragonal unit cell (space group = I4/m) with values between 9.77 and 9.79 Å and 2.85 and 2.87 Å, respectively, were essentially unchanged by the dehydration process, in good agreement with the earlier X-ray and neutron data of Rossouw et al.[15, 41] By contrast, in the XRD study by Johnson et al.,[13] the refined lattice parameters were *a/b* = 9.81 and *c* = 2.85 Å for a hydrated product and *a/b* = 9.75 and *c* = 2.86 Å for a dehydrated product, respectively, showing more pronounced difference between the hydrated and dehydrated products in the a/b lattice parameter. The comparisons reflect small inconsistencies in the published X-ray and neutron data, particularly in the *a/b* value of the dehydrated product mentioned above. The lattice parameters of a dehydrated α-MnO$_2$ sample were therefore obtained, *in situ*, by synchrotron XRD at the APS to determine accurate lattice parameter values for baseline α-MnO$_2$. Since the *in situ* measurement was performed at 400 °C whereas the other measurements were made at 25 °C, however, adjustments need to be made to account for the effect of thermal expansion. Since thermal expansion coefficients are not available for α-MnO$_2$, the values for β-MnO$_2$ were used.[40] The β-MnO$_2$ phase has the additional advantage that the 1×1 tunnels are too small for H$_2$O intercalation, thus ensuring that the temperature dependence of lattice parameter is solely due to thermal expansion. After adjusting for thermal expansion, the baseline lattice parameters for dehydrated α-MnO$_2$ at 25 °C were determined to be *a/b* = 9.79 and *c* = 2.87 Å (Table 1).

In our DFT calculations, the *a/b* and *c* lattice parameters of pure (dehydrated) α-MnO$_2$ were found to be 9.91 Å and 2.93 Å respectively, i.e., 1.2% and 2.0% larger than the respective baseline values (9.79 Å and 2.87 Å) for dehydrated α-MnO$_2$ determined, *in situ*, by synchrotron XRD (Table 1). The volume of the dehydrated unit cell (287.75 Å^3) is over-predicted by 4.5%.

3.3 DFT Model for Volume Changes with Li/Li-oxide Insertion

Despite the discrepancy in nominal lattice parameters between DFT calculations and XRD measurements, DFT calculations can be used to predict increases in unit cell volumes, relative to dehydrated α-MnO_2, as a function of the Li/Li_2O content in the tunnels. Using α-MnO_2 supercells of 8-24 formula units, various quantities of Li and/or Li_2O were inserted into the 2×2 tunnel structure at various configurations to compute the total energy using DFT+U calculations, as described in Section 2.5. A total of 15 $xLi_2O\bullet MnO_2$, 44 Li_yMnO_2, and 101 $xLi_2O\bullet Li_yMnO_2$ structures were considered. For each composition (i.e. each set of x and y), the lowest energy configuration and those with energies within 30 meV/Mn of the lowest were considered likely configurations. The optimized volumes of these structures were compared to that of dehydrated α-MnO_2, and the percentage changes calculated.

Figure 5a shows the DFT-calculated percentage volume change of various $xLi_2O\bullet Li_yMnO_2$ structures, compared to dehydrated α-MnO_2, plotted against the total Li content per Mn. The $xLi_2O\bullet MnO_2$ structures show a nearly linear behavior and were fitted to a least squares straight line through the origin ($\%\Delta V_x = 25.06x$). The Li_yMnO_2 structures exhibit a quadratic dependence on Li content and were fitted to a least square quadratic line through the origin ($\%\Delta V_y = 17.16y^2+5.76y$). The two separate trends in x and y do not adequately predict the volume changes of the mixed $xLi_2O\bullet Li_yMnO_2$ structures. Therefore, a least squares quadratic fit in the variable xy was performed ($\%\Delta V_{xy} = -233.79x^2y^2+45.98xy$) for the residual. The final DFT-based model:

$$\%\Delta V_{total} = 25.06x+17.16y^2+5.76y+233.79x^2y^2+45.98xy \tag{1}$$

predicts on average 101% of the percentage volume change of the mixed $xLi_2O\bullet Li_yMnO_2$ structures, with a correlation coefficient of 0.993 and a root-mean-squared error of 0.66

percentage points. Figure 5b shows the percentage volume change predicted from the DFT-based

model vs the actual DFT-calculated values.
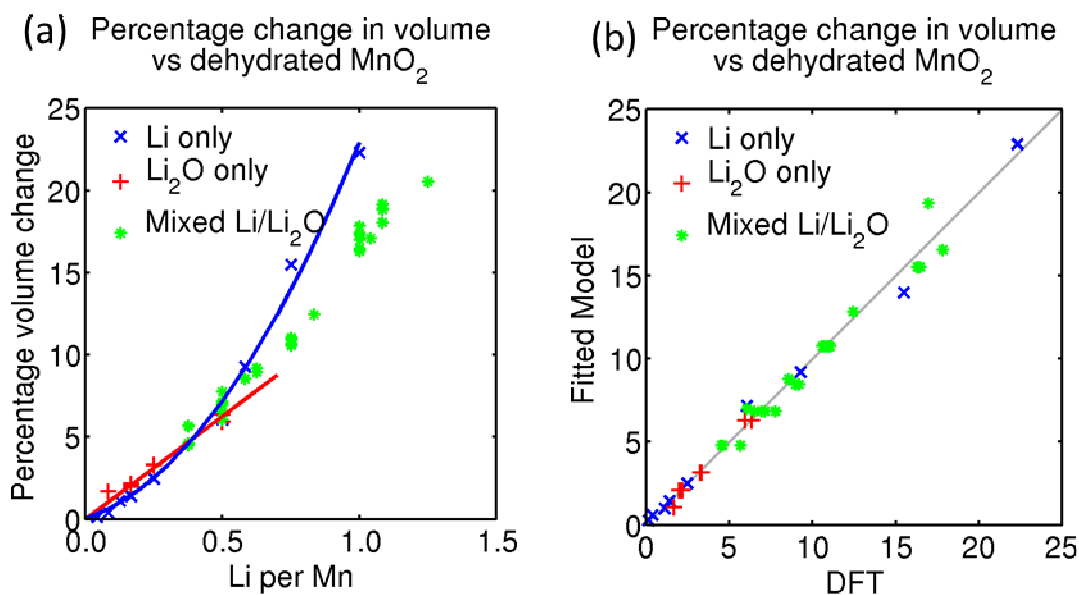
Figure 5. (a) Percentage volume change (relative to dehydrated α-MnO$_2$) of various Li- and Li$_2$O- inserted α-MnO$_2$ structures, as calculated from density functional theory, plotted against Li content. (b) Percentage volume change (relative to dehydrated α-MnO$_2$) of the DFT-based fitted model (Equation 1) vs the calculated values. The DFT-based model allows the prediction of the percentage volume change of xLi$_2$O$\bullet$Li$_y$MnO$_2$ compared to dehydrated α-MnO$_2$ for values of x and y which satisfies x$\leq$0.25 and 2x+y$\leq$1.0.

Using the above DFT-based model (Equation 1), we compare the predicted volume

changes for several compositions with the data for Li$_2$O- and Li-inserted α-MnO$_2$ reported by

Johnson et al.[13] The results are shown in Table 2. Using the baseline volume (for dehydrated α-

MnO$_2$) reported by Johnson et al., the root-mean-squared (RMS) error of the predictions

compared to the experimental measurements is 0.3 percentage points. Using the baseline volume

found in the current work, the RMS error increases to 0.9 percentage points, but the overall trend

is still captured. Overall, the DFT predictions are in reasonably good agreement with the

experimental data.

Table 2. Percentage volume changes of various compositions of Li- and/or Li_2O-inserted MnO_2, relative to dehydrated α-MnO_2, from previous XRD studies[13, 21] and from the DFT-based model described above. Since the baseline volume of dehydrated MnO_2 is substantially different in the current work compared to Ref. 13, both sets of results are presented. Regardless of the baseline volume of dehydrated MnO_2 used, the volumes for Li_2O, Li, and Li_2O+Li inserted MnO_2 were taken from Ref. 13.

Composition	Percentage change in volume (compared to dehydrated α-MnO_2)		
	XRD (baseline from current work)	XRD (baseline from Ref. 13)	DFT-based model
$0.05Li_2O\bullet MnO_2$	0.29	1.35	1.3
$0.10Li_2O\bullet MnO_2$	1.82	2.90	2.5
$0.15Li_2O\bullet MnO_2$	2.96	4.05	3.8
$Li_{0.422}MnO_2$	4.58	5.69	5.5
$0.15Li_2O\bullet Li_{0.26}MnO_2$	7.08	8.22	7.9

3.4 Structural Changes of α-MnO_2 in Electrochemical Cells

3.4.1 Starting electrode in electrochemical cell

Prior to the electrochemical evaluation of the electrodes, an XRD pattern of an α-MnO_2 electrode was obtained, *ex-situ*, after loading the electrode in a Li-O_2 cell after being immersed in the TEGDME electrolyte (data not shown). Refinement of the α-MnO_2 pattern showed a slight expansion (1.4%) of the unit cell with a=b=9.8506Å, c=2.8592Å and cell volume=277.45 Å^3 relative to the partially dehydrated parent electrode material ($0.11H_2O\bullet MnO_2$) with a=b=9.7732Å, c=2.8639Å and cell volume=273.55 Å^3 (Table 1). The increase in the unit cell volume is tentatively attributed to the ion exchange of Li$^+$ from the liquid LiTFSi/TEGDME electrolyte with protons from the occluded H_2O component, which would be consistent with the trend of $xLi_2O\bullet MnO_2$ compositions in Table 1. The measured cell volume is consistent with the predicted, DFT-calculated composition of $xLi_2O\bullet MnO_2$ where x = 0.04 (using the baseline volume from this work) or 0.08 (using the baseline volume from Ref 13).

3.4.2 *In situ* analysis of Li/α-MnO_2−O_2 coin cell

A typical *in situ* XRD data set of a Li/α-MnO$_2$−O$_2$ cell, obtained during an initial discharge and charge over a 20 h period, is shown in Figure 6a. The electrochemical data are presented in a voltage vs. time plot to correlate with the time-resolved XRD patterns, from which the background noise was removed for clarity. The cell was cycled between 2.5 - 4.5 V at 0.05 mA for 10 h per half cycle. The combined XRD and electrochemical data indicate that the cell discharges in three distinct steps: During scans 1-2, the cell voltage decreases sharply from 3.5 to 3.0 V in 30 minutes while, during scans 3-7, the potential decreases gradually to 2.5 V over a 5 h period. Thereafter, during scans 8-12, the cell discharges at approximately 2.5 V for another 5 h. It is clear from the XRD patterns of the first 7 scans that significant changes occur to the α-MnO$_2$ structure during the first two steps.
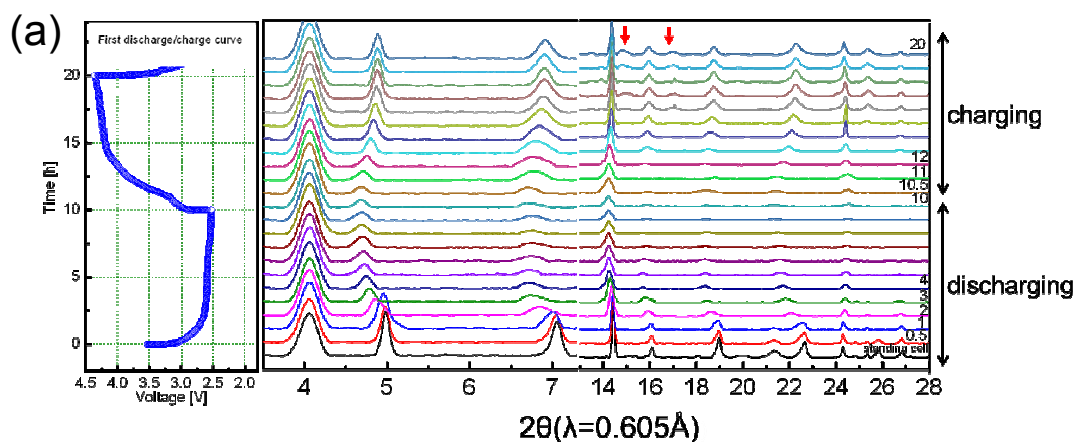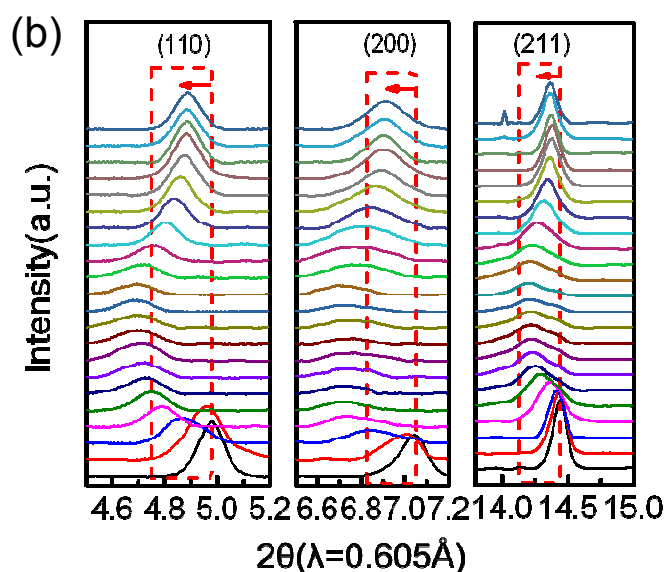
Figure 6. (a) *In situ* XRD patterns (background subtracted) of a Li/α-MnO$_2$−O$_2$ cell during the initial discharge/charge. Patterns were recorded every 30 minutes during discharge/charge, with 2θ ranges 4-8°(left) and 14-28°(right) (partial data provided in the figure). The two red arrows point to peaks to LiF (JCPDS 45-1460). (b) Expanded time-resolved data showing changes in the position and intensity of the (110), (200) and (211) peaks of the tetragonal α-MnO$_2$ unit cell during cycling.

The shift of the α-MnO$_2$ peaks to lower 2θ values (higher d-spacing), i.e., from 4.98 to 4.75 °2θ during the first 7 scans of discharge, indicates an expansion of the unit cell as a result of lithium (and perhaps some oxygen) insertion into the α-MnO$_2$ host structure. These data are consistent with the formation of xLi$_2$O•Li$_y$MnO$_2$ compounds[4, 13, 42] (Table 1) and with previous DFT calculations that have shown that these compounds should be produced electrochemically between 3.0V and 2.7 V relative to a metallic lithium anode.[17, 21, 43]

The voltage plateau at approximately 2.5 V appears to be associated with Li$_2$O$_2$ (and possibly Li$_2$O) formation. However, there was no evidence of crystalline Li$_2$O$_2$ or Li$_2$O products in the synchrotron XRD patterns, even after discharge to 2.0 V on a third cycle, consistent with experiments using Fourier Transform Infrared (FTIR) spectroscopy and Mass Spectroscopy (MS) as probes to detect these products.[44-46] Because DFT calculations reveal that xLi$_2$O•Li$_y$MnO$_2$ compounds are produced close to the electrochemical potential at which Li$_2$O and Li$_2$O$_2$ are

16

formed,[21] these two lithium-oxides cannot be excluded unequivocally as possible intermediate products during the early stages of the electrochemical reaction below 3 V. It is interesting to note, however, that in the absence of α-MnO_2, crystalline Li_2O_2 has been identified as a discharged product in Li-O_2 cells that contain TEGDME-based electrolytes.[47]

In order to examine in more detail the competition between lithium insertion/manganese reduction and oxygen reduction reactions during discharge and, conversely, lithium extraction/manganese oxidation and oxygen oxidation during charge, a 90-h, *in situ* electrochemical experiment was conducted at 0.05 mA whereby changes in the α-MnO_2 lattice parameter values (a=b, c, and cell volume) were monitored *in situ* by synchrotron XRD as a function of the discharge/charge profile (Figure 7a). The figure shows three cycles of a Li/α-$MnO_2$$-$$O_2$ cell (top) with corresponding variations in the lattice parameters of the α-MnO_2 electrode/electrocatalyst (bottom). Table 3 lists the lattice parameters of the α-MnO_2 structure at the start of the experiment and at the end of discharge and charge for each of the three cycles. Figure 7b shows the ranges of total Li and O content during cycling contents as deduced from the DFT-based model described in Section 3.3 and the measured unit cell volume changes. Because both Li_2O and Li-insertion gives rise to volume increase, the amount of Li and O is not uniquely defined. However, it is possible to constrain the amount of Li to within approximately ~20% at all points of electrochemical cycling, thus revealing the variations of Li-content during cycling. Since the effect of oxygen on volume is more subtle than that of Li, this analysis is less effective in narrowing the range of O content, and only a probable increase during the first discharge and possible decrease at the very end of charge can be deduced.
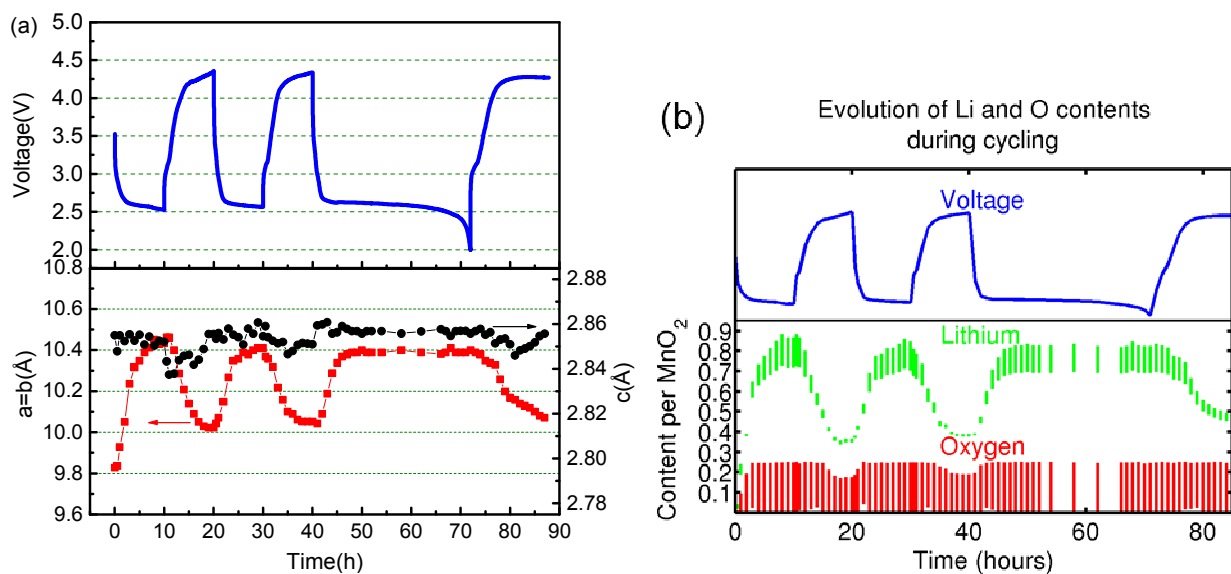
Figure 7. (a) Three cycles of a Li/α-MnO$_2$−O$_2$ cell (top) during which the lattice parameter of the α-MnO$_2$ electrode/electrocatalyst were determined, *in situ*, by synchrotron XRD (bottom). (b) Changes in Li (green) and O (red) contents during cycling as deduced from XRD measurements and DFT-based model.

Table 3. Variation in the cell parameters of a α-MnO$_2$ electrode in a Li/O$_2$ cell at the end of discharge and top of charge - first three cycles.

State of Charge	a=b (Å)	c (Å)	Cell Volume (Å^3)
Starting electrode (in cell)	9.8280	2.8550	275.76
End of 1st discharge	*10.4340*	*2.8521*	*310.50*
Top of 1st charge	10.0233	2.8556	286.89
End of 2nd discharge	*10.4097*	*2.8546*	*309.33*
Top of 2nd charge	10.0521	2.8510	288.08
End of 3rd discharge	*10.3994*	*2.8558*	*308.84*
Top of 3rd charge	10.0712	2.8557	289.65

The changes in the lattice parameters in Figure 7 and Table 3 clearly demonstrate that the α-MnO$_2$ structure participates in the redox activity of the electrochemical cell; they also show that the expansion/contraction of the α-MnO$_2$ unit cell during cycling is substantially anisotropic and that the lattice parameters, calculated by Rietveld refinement with GSAS software, are highly correlated with the electrochemical process, at least during the first two, 10-hour cycles (Figure 7).

During the initial 10-h discharge of the Li/α-MnO$_2$−O$_2$ to approximately 2.5 V, the *a/b* lattice parameter increases significantly from 9.8280 to 10.4340 Å with minimal change to *c* parameter (~2.85 Å); the volume expands by 12.5%. The Li content at the end of first discharge as deduced from the DFT-based model is ~0.8 per Mn, as compared to ~0.1 per Mn at the beginning of electrochemical cycling. During the subsequent 10-h charge to approximately 4.3 V, it is evident that not all the lithium is extracted from the electrode because *a/b* contracts only to 10.0233 Å while the corresponding cell volume decreases by 8.2%, indicating that another electrochemical process occurs during the 10-h charge to compensate for the diminished capacity supplied by the α-MnO$_2$ electrode structure. In fact, after the first discharge, it appears that subsequent charge cycles never reduce the Li content to below ~0.35 per MnO$_2$. On the subsequent 2 cycles, the a/b lattice parameter at the end of discharge decreases steadily, while increasing at the top of charge – a manifestation that the redox activity of the α-MnO$_2$ electrode continues to decline on cycling, which we attribute tentatively to the formation of lithium oxide products at the surface of the α-MnO$_2$ electrode particles, thereby clogging the pores at the surface and preventing easy transport of Li$^+$ ions in and out of the '2×2' channels during discharge and charge. Indeed, allowing the cell to discharge without a time restraint to 2.0 V on the 3rd discharge results in a voltage plateau at ~2.6 V, which is consistent with Li$_2$O$_2$ (and Li$_2$O) formation (Figure 7a, bottom). Of particular significance, is the lattice parameter vs. time plot of the 3rd discharge in Figure 7a (bottom) – it shows an initial rapid increase of *a/b* from to 10.0521 to 10.3994 Å (Table 1), consistent with the insertion of lithium into the α-MnO$_2$ electrode structure. Thereafter, there is a negligible change in *a/b* value for the remainder of discharge (~25 h) to 2.0 V, and correspondingly little to no change in Li and O contents in MnO$_2$, which is fully consistent with the formation of a lithium-oxide product at the MnO$_2$ surface. Although, on average, there is little change to the *c* parameter during cell cycling, noticeable changes do occur

towards the top of charge, when *c* contracts slightly. We conclude, therefore, that the data show a dual functioning electrode that operates via formal redox reactions involving both manganese ions (Li-ion behavior) and oxygen ions (Li-O$_2$ behavior).

It is evident from Figure 7b that there is considerable uncertainty in the amount of oxygen present in the 2×2 tunnels throughout electrochemical cycling. One feature in the DFT-based model (Equation 1) is that for total Li content (2x+y) of less than 0.4 per Mn, volume changes are (a) higher for higher oxygen content, and (b) not strongly dependent on oxygen content, whereas for higher Li contents, the reverse is true on both points. This feature results in large uncertainties in oxygen contents except at the end of charge, where the data is consistent with oxygen release. Additional measurements, e.g. that of Mn oxidation state from x-ray absorption near-edge spectra (XANES), are necessary in order to ascertain the precise mix of Li- vs. Li$_2$O-insertion. The results from XANES and EXAFS spectra have shown an oxidation state self-switching behavior occurring due to a combined Li$^+$ and lithium oxide insertion mechanism when cycled in O$_2$.[25]

3.4.3 *In situ* analysis of a Li/α-MnO$_2$ coin cell

The electrochemical profile and corresponding *in situ* XRD data for the initial discharge/charge cycle of a Li/α-MnO$_2$ cell assembled under argon, when discharged to 2.2 V and charged to 4.4 V at 0.05 mA, are shown in Figure 8a; background noise in the XRD patterns was removed for clarity. Unlike the Li/α-MnO$_2$−O$_2$ cell which showed a distinct voltage plateau during discharge at 2.5 V (Figure 6a), discharge of the Li/α-MnO$_2$ cell occurred with decreasing voltage consistent with topotactic lithium insertion into the α-MnO$_2$ electrode structure over the entire discharge, as described previously by others.[13, 15, 21]

For the electrochemical evaluation of the standard Li/α-MnO$_2$, the α-MnO$_2$ electrode was deliberately not fully dehydrated to maintain the stabilizing effect of the H$_2$O component on the

α-MnO$_2$ structure. Neutron and X-ray refinements have thus far demonstrated that the O content at the center of the 2×2 channels of the structure with a site occupancy between 0.15 and 0.20 (see Section 3.1). Johnson et al. have demonstrated that a lithia-stabilized electrode,[13] 0.15Li$_2$O•MnO$_2$, in which the manganese ions are initially tetravalent, delivers a capacity of 195 mAh/g during the initial discharge to 2.0 V at 0.1 mA. Assuming this to be close to the theoretical capacity, this value would correspond to the uptake of approximately 0.7 Li per 0.15Li$_2$O•MnO$_2$ unit (as well as an ion-exchanged 0.15H$_2$O•MnO$_2$ unit). A fully discharged 0.15Li$_2$O•MnO$_2$ electrode would, therefore, have the composition 0.15Li$_2$O•Li$_{0.7}$MnO$_2$ (or LiMnO$_{2.15}$) in which the average manganese oxidation state is 3.3+, implying the structure would be Jahn-Teller distorted because of the relatively high concentration of Mn^{3+} (d^4) ions. In this respect, the *in situ* XRD data of both Li/α-MnO$_2$−O$_2$ and Li/α-MnO$_2$ cells in Figures 6 and 8, respectively, show considerable peak broadening during discharge and sharpening during charge, consistent with the onset and weakening of the Jahn-Teller effect as lithium is inserted into, and withdrawn from the structure. Other strain effects, such as those induced by particle size effects, are also likely to contribute to line broadening. The excessive line broadening and a diffuse splitting of the peaks (highlighted by the arrow in Figure 8a), which was attributed to a Jahn-Teller-induced phase change, unfortunately prevented meaningful analyses of the lattice parameter changes in the α-MnO$_2$ electrode in the Li/α-MnO$_2$ cell (Figure 8a).
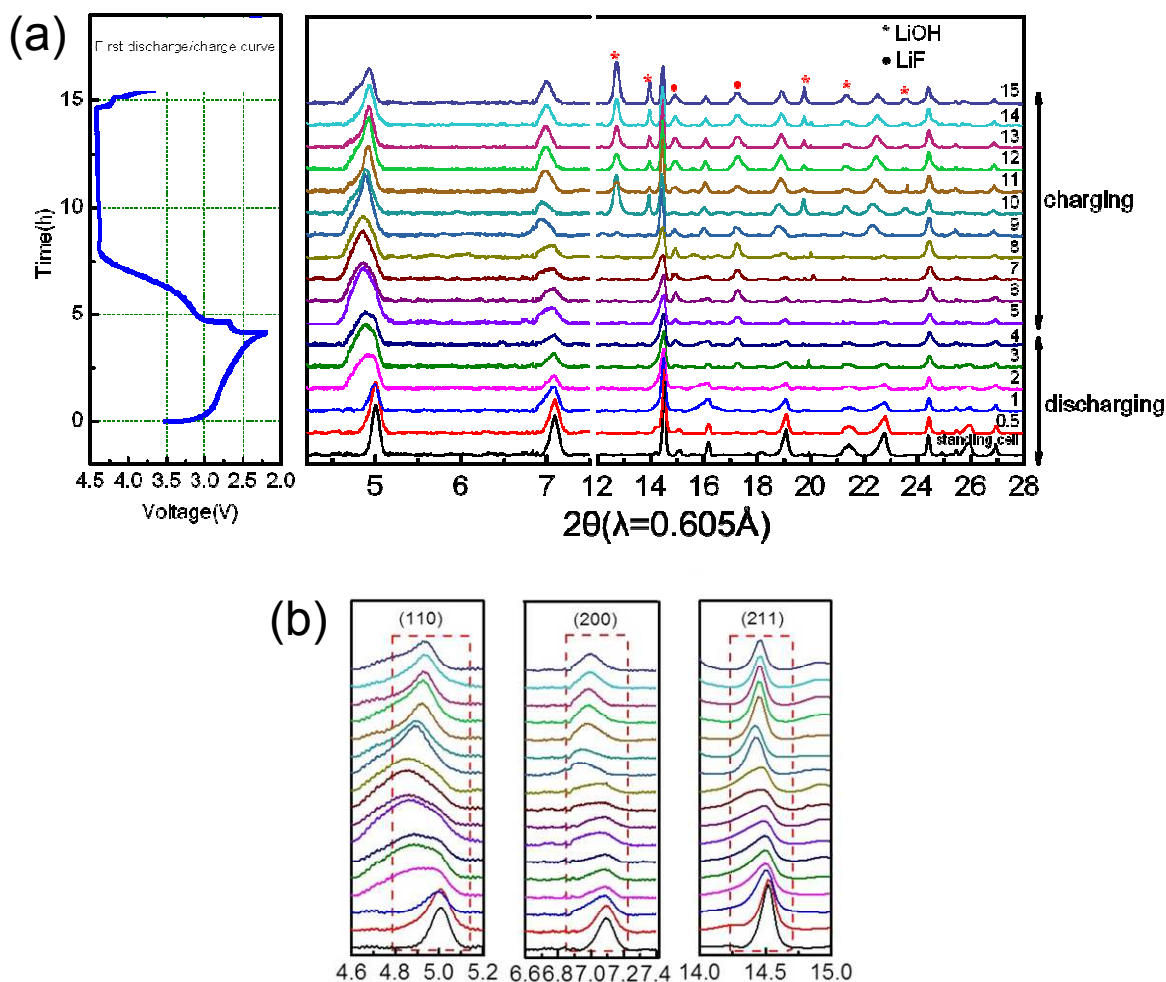
Figure 8. (a) *In situ* XRD patterns (background subtracted) of a Li/α-MnO₂ cell during the initial discharge/charge using the same electrode material and same cycling program as in the Li/α-MnO₂−O₂ cell (Figure 6). Patterns were recorded every 30 minutes during discharge/charge, with 2θ ranges 4-8°(left) and 14-28°(right) (partial data provided in the figure). (b) Expanded time-resolved data showing changes in the position and intensity of the (110), (200) and (211) peaks of the tetragonal α-MnO₂ unit cell during cycling.

Finally, it is noteworthy that LiOH and LiF side-products form during charge and discharge, most noticeably when the $Li/0.15Li_2O \cdot MnO_2$ cell is charged continuously above 4 V; these products are tentatively attributed to electrolyte-induced reactions[48] due to prolonged oxidation at high voltage, and is a topic for future study.

4. Conclusions

α-MnO$_2$ has been studied, *in situ*, by high energy, synchrotron X-ray diffraction as an electrode in Li/α-MnO$_2$−O$_2$ and conventional Li/α-MnO$_2$ coin cells during electrochemical cycling. Density functional theory modeling has been used to quantify the evolution of Li and O contents in the 2×2 tunnels in the structure of α-MnO$_2$ during cycling. The α-MnO$_2$ unit cell expands and contracts anisotropically as a result of lithium insertion/extraction reactions, as expected, and the electrode particles undergo strain during cycling. These reactions are partially reversible, with the electrode cycling between ~0.35 to ~0.8 Li per MnO$_2$ after the first cycle. When operated under oxygen, competing reactions occur between lithium and the oxygen electrode, most noticeably during discharge below ~2.6 V, thereby giving the cell both Li-ion and Li-O$_2$ character. No evidence of crystalline Li$_2$O$_2$ or Li$_2$O formation was apparent from the synchrotron data, suggesting that the α-MnO$_2$ plays a role in the oxygen reduction reaction. Because of the relative insensitivity of unit cell volume to oxygen content at high Li contents, a question that still remains is the extent to which oxygen is removed from, and reinserted into, the '2×2' tunnels of a xLi$_2$O•α-MnO$_2$ (or xH$_2$O•α-MnO$_2$) electrode structure during charge and discharge, respectively, in a Li-O$_2$ cell. Further characterizations are required to fully explore the extent of concomitant Li- and 'Li$_2$O'-insertion into MnO$_2$.

Acknowledgements

References

1   K. M. Abraham and Z. Jiang, *J. Electrochem.Soc.*, 1996, **143**, 1.
2   P. G. Bruce, S. A. Freunberger, L. J. Hardwick, and J.-M. Tarascon, *Nat. Mater.*, 2012, **11**, 19.
3   J. Christensen, P. Albertus, R. S. Sanchez-Carrera, T. Lohmann, B. Kozinsky, R. Liedtke, J. Ahmed, and A. Kojic, *J. Electrochem. Soc.*, 2012, **159**, R1.
4   M. M. Thackeray, M. K. Y. Chan, L. Trahey, S. Kirklin, and C. Wolverton, *J. Phys. Chem. Lett.*, 2013, **4**, 3607.
5   C. Tran, X. Q. Yang, and D. Qu, *J. Power Sources*, 2010, **195**, 2057.
6   R. E. Williford and J.-G. Zhang, *J. Power Sources*, 2009, **194**, 1164.
7   Y. Shao, S. Park, J. Xiao, J. Zhang, Y. Wang, and J. Liu, *ACS Catal.*, 2012, **2**, 844.
8   A. Kraytsberg and Y. Ein-Eli, *J. Power Sources*, 2011, **196**, 886.
9   A. Debart, J. Bao, G. Armstrong, and P. G. Bruce, *J. Power Sources*, 2007, **174**, 1177.
10   A. Debart, A. J. Paterson, J. Bao, and P. G. Bruce, *Angew. Chem. Int. Ed.*, 2008, **47**, 4521.
11   V. Giordani, S. A. Freunberger, P. G. Bruce, J. M. Tarascon, and D. Larcher, *Electrochem. Solid State Lett.*, 2010, **13**, A180.
12   L. Trahey, C. S. Johnson, J. T. Vaughey, S. H. Kang, L. J. Hardwick, S. A. Freunberger, P. G. Bruce, and M. M. Thackeray, *Electrochem. Solid State Lett.*, 2011, **14**, A64.
13   C. S. Johnson, D. W. Dees, M. F. Mansuetto, M. M. Thackeray, D. R. Vissers, D. Argyriou, C. K. Loong, and L. Christensen, *J. Power Sources*, 1997, **68**, 570.
14   C. S. Johnson and M. M. Thackeray, *J. Power Sources*, 2001, **97-8**, 437.
15   M. H. Rossouw, D. C. Liles, M. M. Thackeray, W. I. F. David, and S. Hull, *Mater. Res. Bull.*, 1992, **27**, 221.
16   M. M. Thackeray, *Prog. Solid St. Chem.*, 1997, **25**, 1.
17   D. A. Tompsett and M. S. Islam, *Chem. Mater.*, 2013, **25**, 2515.
18   D. A. Tompsett, S. C. Parker, and M. S. Islam, *J. Mater. Chem. A*, 2014, **2**, 15509.
19   D. A. Tompsett, S. C. Parker, P. G. Bruce, and M. S. Islam, *Chem. Mater.*, 2013, **25**, 536.
20   T. T. Truong, Y. Liu, Y. Ren, L. Trahey, and Y. Sun, *ACS Nano*, 2012, **6**, 8067.
21   L. Trahey, N. K. Karan, M. K. Y. Chan, J. Lu, Y. Ren, J. Greeley, M. Balasubramanian, A. K. Burrell, L. A. Curtiss, and M. M. Thackeray, *Adv. Energy Mater.*, 2013, **3**, 75.
22   X. Hu, X. Han, Y. Hu, F. Cheng, and J. Chen, *Nanoscale*, 2014, **6**, 3522.
23   Z. H. Lu and J. R. Dahn, *J. Electrochem. Soc.*, 2002, **149**, A815.
24   X. Q. Yang, J. McBreen, W.-S. Yoon, and C. P. Grey, *Electrochem. Commun.*, 2002, **4**, 649.
25   G. S. Hutchings, J. Rosen, D. Smiley, G. R. Goward, P. G. Bruce, and F. Jiao, *J. Phys. Chem. C*, 2014, **118**, 12617.
26   K. R. Ryan, L. Trahey, J. S. Okasinski, A. K. Burrell, and B. J. Ingram, *J. Mater. Chem. A*, 2013, **1**, 6915.
27   A. P. Hammersley, S. O. Svensson, M. Hanfland, A. N. Fitch, and D. Hausermann, *High Pressure Res.*, 1996, **14**, 235.
28   A. C. Larson and R. B. Von Dreele, *LosAlamos National Laboratory Report LAUR*, 2004, 86.
29   B. H. Toby, *J. Appl. Cryst.*, 2001, **34**, 210.
30   G. Kresse and J. Furthmüller, *Phys. Rev. B*, 1996, **54**, 11169.
31   G. Kresse and D. Joubert, *Phys. Rev. B*, 1999, **59**, 1758.

32   J. P. Perdew, M. Ernzerhof, and K. Burke, *J. Chem. Phys.*, 1996, **105**, 9982.

33   S. L. Dudarev, G. A. Botton, S. Y. Savrasov, C. J. Humphreys, and A. P. Sutton, *Phys. Rev. B*, 1998, **57**, 1505.

34   M. Chan and J. Greeley, *unpublished*, 2013.

35   A. Bystrom and A. M. Bystrom, *Acta Cryst.*, 1950, **3**, 146.

36   T. Ohzuku, M. Kitagawa, K. Sawai, and T. Hirai, *J. Electrochem. Soc*, 1991, **138**, 360.

37   M. H. Rossouw and M. M. Thackeray, *US Patent*, 1992, **5,166,012**.

38   H. Miura, *Minera. J.*, 1986, **13**, 119.

39   S. Ishiwata, J. W. G. Bos, Q. Huang, and R. J. Cava, *J. Phys.: Condens. Matter*, 2006, **18**, 3745.

40   R. C. Bradt and J. S. Wiley, *J. Electrochem. Soc.*, 1962, **109**, 651.

41   M. Rossouw, A. de Kock, L. de Picciotto, M. Thackeray, W. David, and R. Ibberson, *Mat. Res. Bull.*, 1990, **25**, 173.

42   S. Devaraj and N. Munichandraiah, *J. Phys. Chem. C*, 2008, **112**, 4406.

43   C. Ling and F. Mizuno, *Chem. Mater.*, 2012, **24**, 3943.

44   F. Mizuno, S. Nakanishi, Y. Kotani, S. Yokoishi, and H. Iba, *Electrochemistry*, 2010, **78**, 403.

45   W. Xu, V. V. Viswanathan, D. Wang, S. A. Towne, J. Xiao, Z. Nie, D. Hu, and J.-G. Zhang, *J. Power Sources*, 2011, **196**, 3894.

46   S. A. Freunberger, Y. Chen, Z. Peng, J. M. Griffin, L. J. Hardwick, F. Barde, P. Novak, and P. G. Bruce, *J. Am. Chem. Soc.*, 2011, **133**, 8040.

47   C. O. Laoire, S. Mukerjee, E. J. Plichta, M. A. Hendrickson, and K. M. Abraham, *J. Electrochem. Soc.*, 2011, **158**, 302.

48   S. Meini, S. Solchenbach, M. Piana, and H. A. Gasteiger, *J. Electrochem. Soc.*, 2014, **161**, A1306.